Knowledge-Augmented Contrastive Learning for Abnormality Classification and Localization in Chest X-rays with Radiomics using a Feedback Loop

Yan Han[1], Chongyan Chen[1], Ahmed Tewfik[1], Benjamin Glicksberg[2], Ying Ding[1], Yifan Peng[3]†, Zhangyang Wang[1]‡
[1]The University of Texas at Austin, [2]Icahn School of Medicine at Mount Sinai, [3]Weill Cornell Medicine
†yip4002@med.cornell.edu, ‡atlaswang@utexas.edu

Abstract

Accurate classification and localization of abnormalities in chest X-rays play an important role in clinical diagnosis and treatment planning. Building a highly accurate predictive model for these tasks usually requires a large number of manually annotated labels and pixel regions (bounding boxes) of abnormalities. However, it is expensive to acquire such annotations, especially the bounding boxes. Recently, contrastive learning has shown strong promise in leveraging unlabeled natural images to produce highly generalizable and discriminative features. However, extending its power to the medical image domain is under-explored and highly non-trivial, since medical images are much less amendable to data augmentations. In contrast, their prior knowledge, as well as radiomic features, is often crucial. To bridge this gap, we propose an end-to-end semi-supervised knowledge-augmented contrastive learning framework, that simultaneously performs disease classification and localization tasks. The key knob of our framework is a unique positive sampling approach tailored for the medical images, by seamlessly integrating radiomic features as a knowledge augmentation. Specifically, we first apply an image encoder to classify the chest X-rays and to generate the image features. We next leverage Grad-CAM to highlight the crucial (abnormal) regions for chest X-rays (even when unannotated), from which we extract radiomic features. The radiomic features are then passed through another dedicated encoder to act as the positive sample for the image features generated from the same chest X-ray. In this way, our framework constitutes a feedback loop for image and radiomic features to mutually reinforce each other. Their contrasting yields knowledge-augmented representations that are both robust and interpretable. Extensive experiments on the NIH Chest X-ray dataset demonstrate that our approach outperforms existing baselines in both classification and localization tasks.

1. Introduction

The chest X-ray is one of the most common radiological examinations for detecting cardiothoracic and pulmonary abnormalities. Due to the demand for accelerating chest X-ray analysis and interpretation along with the overall shortage of radiologists, there has been a surging interest in building automated systems of chest X-ray abnormality classification and localization [28]. While the class (i.e., outcomes) labels are important, the localization annotations, or the tightly-bound local regions of images that are most indicative of the pathology, often provide richer information for clinical decision making (either automated or human-based).

Automatic robust image analysis of chest X-rays currently faces many challenges. First, recognizing abnormalities in chest X-rays often requires expert radiologists. This process is therefore time-consuming and expensive to generate annotations for chest X-ray data, in particular the localized bounding box region labeling. Second, unlike natural images, chest X-rays have very subtle and similar image features. The most indicative features are also very localized. Therefore, chest X-rays are sensitive to distortion and not amendable to typical image data augmentations such as random cropping or color jittering. Moreover, in addition to high inter-class variance of abnormalities seen in chest X-rays (i.e., feature differences between different diseases), chest X-rays also have large intra-class variance (i.e., differences in presentation among individuals of the same diseases). The appearance of certain diseases in X-rays are often vague, can overlap with other diagnoses, and can mimic many other benign abnormalities. Last but not least, the class distribution of chest X-rays is also highly imbalanced for available datasets.

Recently, contrastive learning has emerged as the frontrunner for self-supervised learning, demonstrating superior ability to handle unlabelled data. Popular frameworks in-

clude MoCo [14, 6], SimCLR [4, 5], PIRL [22] and BYOL [12]. They all have achieved prevailing success in natural image machine learning tasks, such as image classification and object detection. Further, contrastive learning appears to be robust for semi-supervised learning when only few labeled data are available [5]. Recent works also found contrastive learning to be robust to data imbalance [37, 17].

Contrastive learning may offer a promising avenue for learning from the mostly unlabeled chest X-rays, but leveraging it for this task is not straightforward. One most important *technical barrier* is that most contrastive learning frameworks [14, 6, 4, 5, 12] critically depend on maximizing the similarity between two "views", i.e., an anchor and its **positive sample**, often being generated by applying random data augmentations to the same image. This data augmentation strategy, however, does not easily translate to chest X-rays. In addition, the simultaneous demand for both classification and localization-aware features further complicates the issue. Fortunately, classical chest X-ray analysis has introduced **radiomic features** [7] as an auxiliary knowledge augmentation. The radiomic features can be considered as a strong *prior*, and therefore can potentially be utilized to guide learning of deep feature extractors. However, the extraction of reliable radiomic features via Pyradiomic[1] tool [34] heavily depends on the pathology localization – hence we will run into an intriguing "chicken-and-egg" problem, when trying to incorporate radiomic features into contrastive learning, whose goal includes learning the localization from unlabeled data.

This paper presents an innovative holistic framework of **Knowledge-Augmented Contrastive Learning**, which seamlessly integrates radiomic features as the other contrastive knowledge-augmentation for the chest X-ray image. As the *main difference* from existing frameworks, the two "views" that we contrast now are from two different domain knowledge characterizing the same patient: the chest X-ray image and the radiomic features. Notably, the radiomic features have to be extracted from the learned pathology localizations, which are not readily available. As these features will be dynamically updated, forming a "feedback loop" during training in which both modalities' learning mutually reinforce each other. The *key enabling technique* to link this feedback loop is a novel module we designed, called *Bootstrap Your Own Positive Samples* (**BYOP**). For an unannotated X-ray image, we utilize Grad-CAM [30] to generate the input heatmap from the image modality backbone, which yields the estimated bounding box after thresholding; and we then extract the radiomic features within this estimated bounding box, which becomes the alternative view to contrast with the image view. The usage of radiomic features also adds to the model interpretability. Our contributions are outlined as follows:

[1] https://pyradiomic.readthedocs.io/

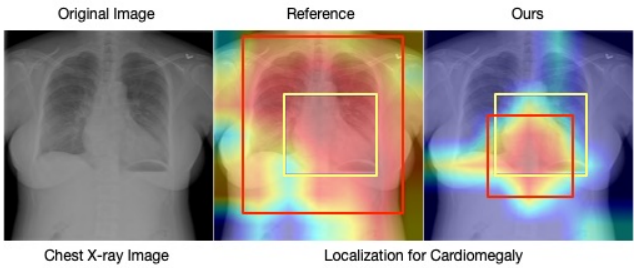


Figure 1. Visualization of heatmaps of chest X-rays with ground-truth bounding box annotations (yellow) and its prediction (red) for localize Cardiomegaly in one test chest X-ray image. The visualization is generated by rendering the final output tensor as heatmaps and overlaying it on the original images. The left image is the original chest X-ray image, the middle is the visualization result by CheXNet [28] and the right is our model's attempt. Best viewed in color.

- A brand-new **framework** dedicated to improving abnormality identification and localization in (mostly unannotated) chest X-rays by knowledge-augmented contrastive learning, which highlights exploiting radiomic features as the auxiliary knowledge augmentation to contrast with the images, given the inability to perform classical image data augmentation.
- An innovative **technique** called BYOP to enable the effective generation of radiomic features, which is necessary as the true bounding boxes are often absent. BYOP leverages an interpretable learning technique to supply estimated bounding boxes dynamically during training.
- Excellent experimental **results** achieved on the NIH Chest X-ray benchmark [35], using very few annotations. Besides improving the disease classification AUC from 82.8% to 83.8%, our framework significantly boosts the localization results, by an average of 2% over different IoU thresholds, compared to reported baselines. Figure 1 provides a visualization example showing our localization results to be more robust and accurate than the previous results from CheXNet [28],

2. Related Work

Self-supervised Learning and Contrastive Learning: Self-supervision uses pre-formulated (or "pretext") tasks to train with unlabeled data. Popular handcrafted pretext tasks include solving jigsaw puzzles [24], relative patch prediction [8] and colorization [41]. However, many of these tasks rely on ad-hoc heuristics that could limit the generalization and transferability of learned representations. Consequently, contrastive learning of visual representations has emerged as the front-runner for self-supervision and has demonstrated superior performance on downstream tasks [14, 6, 4, 5, 22, 12]. Most of those successes take place

in the natural image domain due to the ease of creating contrastive views by applying data augmentations.

There have been a few recent attempts towards contrastive learning in multi-domain knowledge tasks. [33] studied knowledge transfer via contrastive learning, including from one sensory domain knowledge to another (e.g., RGB to Depth). [27] contrasted bright-field and second-harmonic generation microscopy images for their registration: two image domain knowledge captured for biomedical applications, with large appearance discrepancy between them. [40] aimed to learn text-to-image synthesis by maximizing the mutual information between image and text, through multiple contrastive losses which capture inter-domain and intra-domain correspondences. The commodity among those existing works is that their two domains (e.g., image and text, RGB and depth, or two types of microscopy images) are both readily available for training. **In contrast to our task**, the other radiomic features domain knowledge is not available ahead of training and needs to be adaptively bootstrapped from the image domain during training.

Contrastive Learning for Medical Image Analysis: Self-supervised learning using pre-text tasks has been recently popular in medical image analysis [32, 1, 45, 46, 15]. When it comes to contrastive learning, [3] proposed a domain-specific pretraining strategy, by extracting contrastive pairs from MRI and CT datasets using a combination of localized and global loss functions, which relies on the availability of both MRI and CT scans. [43] leveraged contrastive learning to infer transferable medical visual representations from paired images and text modalities.

Prior work adopting contrastive learning on chest X-rays remains scarce, due to the roadblock of creating two contrastive views. [20] explicitly contrasted X-rays with pathologies against healthy ones using attention networks, in a fully supervised setting. The closest recent work to our knowledge [13] also applied radiomic features to guide contrastive learning for detecting pneumonia in chest X-rays. However, their method needs to apply a pre-trained ResNet on the images to generate attention for radiomic features extraction and therefore relied on a multi-stage training heuristic. Their method hence produced no joint optimization of two domain knowledge, and lacked the localization capability.

Radiomics in Medical Diagnosis: Radiomics studies have demonstrated their power in image-based biomarkers for cancer staging and prognostication [23]. Radiomics extracts quantitative data from medical images to represent tumor phenotypes, such as spatial heterogeneity of a tumor and spatial response variations. [9] demonstrated that radiomic of CT texture features are associated with the overall survivalrate of pancreatic cancer. [7] revealed that the first-order radiomic features (e.g., mean, skewness, and kurtosis) are correlated with pathological responses to cancer treatment. [16] showed that radiomics could increase the positive predictive value and reduce the false-positive rate in lung cancer screening for small nodules compared with human reading by thoracic radiologists. [42] found that multiparametric MRI-based radiomics nomograms provided improved prognostic ability in advanced nasopharyngeal carcinoma (NPC). In comparison, deep learning algorithms are often criticized for being "black box" and lack interpretability despite high predictive accuracy. That limitation has motivated many interpretable learning techniques including activation maximization [10], network inversion [21], GradCAM [30], and network dissection [2]. We believe that the joint utilization of radiomics and interpretable learning techniques in our framework can further advance accurate yet interpretable learning in the medical image domain.

3. Method

The Framework. Our goal is to learn an image representation y_i which can then be used for disease classification and localization. Our framework uses two neural networks to learn: the image and radiomics networks. The image network consists of an encoder f_i (ResNet-18) and a projector g_i (two-layer MLPs with ReLU). The radiomics network has a similar architecture as the image network, but uses another three-layer MLPs for radiomic encoder f_r and a different set of weights for the projector g_r. The proposed architecture is summarized in Figure 2.

The primary innovation of our method lies in how we select positive and negative examples, which will be expanded below in Section 3.1 and Section 3.2. We also formulate the semi-supervised loss for our problem when a small amount of annotated data is available in Section 3.3. The entire framework can be trained from end to end, and the representation y_i will be used for downstream disease classification and localization tasks.

3.1. Finding Positive and Negative Samples: Data-Driven Learning Meets Domain Expertise

The reasons to use contrastive learning as our framework are three-fold. First, contrastive learning leverages unlabeled data and we have few disease localization (bounding boxes) annotations available. Second, empirical findings [37, 17] prove that contrastive learning is robust in classification tasks with class-imbalanced datasets. In clinical settings, most medical image datasets suffer an extreme class-imbalance problem [11]. Third, contrastive learning naturally fits "multi-view" concepts. In our case, we are still comparing two different views of the same subject, but unlike classic contrastive learning where two views are from the same domain space, our views for positive sampling are from different domain knowledge ([39] proved that views from multi-domain knowledge should also align), while our

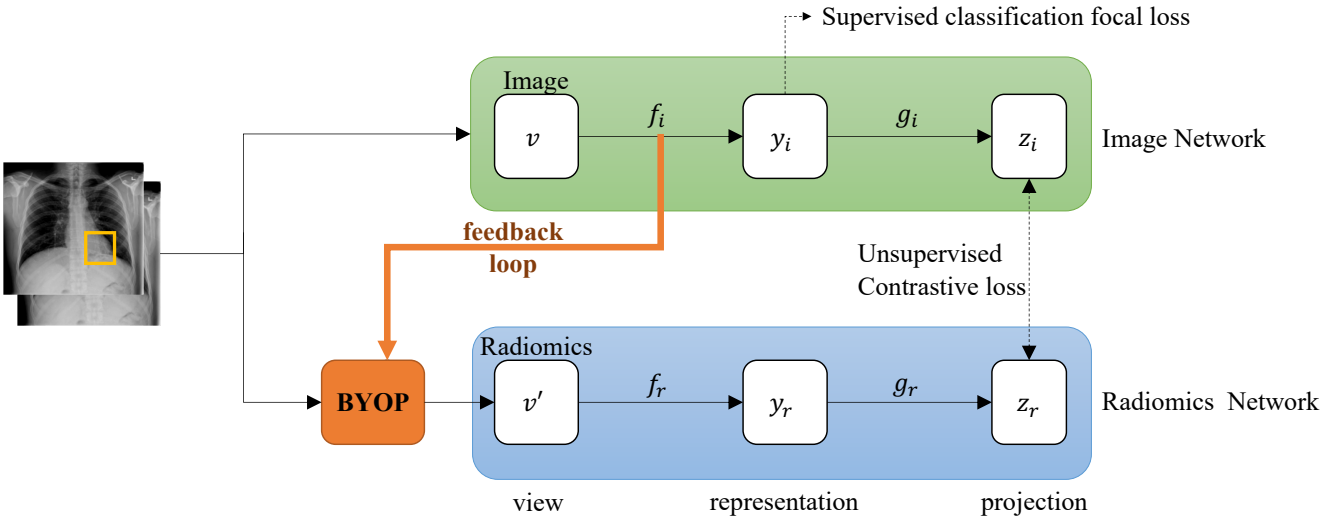


Figure 2. Overview of our proposed framework. During training, given a set of images, very few images have annotations, our framework provides two views: the image and the radiomic features (generated by the BYOP module, the detail view is shown in Figure 3). From the image view v, we output a representation $y_i = f_i(v)$ and a projection $z_i = g_i(y_i)$ via an image encoder f_i and image projection head g_i, respectively. Similarly, from the radiomic view v', we output $y_r = f_r(v')$ and the radiomic projection $z_r = g_r(y_r)$ via a radiomic encoder f_r and radiomic projection head g_r, respectively. We maximize agreement between z_i and z_r via a contrastive loss (NT-Xnet). In addition, we minimize the classification errors from representation y_i via a focal loss. During testing, only the image encoder is kept and applied to the new X-rays.

negative sampling is from the same domain knowledge. In the subsequent section, we will describe our unique positive and negative sampling methodologies in more detail.

Positive Sampling. To obtain a positive pair of views, we randomly select an image labeled with a given disease and generate two views for it. The first view will be its image features and another view will be its radiomic features. We decided to leverage radiomic features for the second view as traditional image augmentation strategies cannot be leveraged here. Furthermore, radiomic features have labels, are naturally more interpretable than the image features extracted from deep learning-based image encoders.

Obtaining the radiomic features for our dataset is a "chicken-and-egg" problem. **Radiomic features are highly sensitive and dependent on local regions** for which we do not have local bounding box annotations. Meanwhile, we need to make the image features similar to the radiomic features to learn from radiomic features to better learn localization of the abnormalities. This process means that **bounding boxes generation is dependent on radiomic features** which forms a loop cycle. To address this issue, we design the *Bootstrap Your Own Positive Samples* (**BYOP**) method using such a feedback module. For more details, see Section 3.2.

Negative Sampling. The original images are used for views of the negative samples because the same domain is supposed to be more similar and thus harder for the model to distinguish between the positive and negative samples, leading to a more robust model [29]. Besides, the image features focuses on local regions highlighted by the attention map rather than the whole image. To identify harder negative samples, we go one step further, by not only selecting any random image, but "hard similar" images. Here, we first get prior knowledge from the pre-constructed disease hierarchy relationship for image negative sampling, shown in Figure 4, defined by [44]. The pre-constructed disease hierarchy relationship is initialed with 21 nodes. In this hierarchy, each disease (green) belongs to a body part (grey). We therefore only treat normal chest X-rays or images within the same body part but with a different disease as negative examples. We call these negative examples "hard similar" images in this study. As an example, if our "anchor" image is labeled as "Pneumonia/Lung" , our "hard similar" images should include "Atelectasis/Lung", "Edema/Lung", or "Normal" but not "Bone Fractures".

3.2. Bootstrap Your Own Positive Samples (BYOP) with Radiomics in the Feedback Loop

The core component of our cross-modal contrastive learning is the *Bootstrap Your Own Positive Samples* (**BYOP**) module. BYOP leverages a feedback loop to learn region localization from generated radiomic features as the positive sample for the image features. The architecture of BYOP is shown in Figure 3. The BYOP contains two components, bounding box generation and radiomic features extraction.

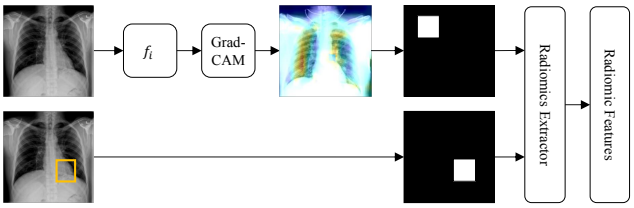


Figure 3. Overview of our *BYOP module*. For the unannotated images, we leverage *Grad-CAM* to generate heatmaps and apply an ad-hoc threshold to generate the bounding boxes. For the annotated images, we directly use the ground-truth bounding boxes. Then with the combination of generated bounding boxes and ground-truth bounding boxes, we use the *Pyradiomic* tool as the radiomic extractor to extract the radiomic features. Note that the generated radiomic features are the combination of the accurate and 'pseudo' radiomic features for annotated and unannotated images, respectively.

Bounding Boxes Generation. We feed the fourth layer of the image encoder f_i (i.e., ResNet-18) to the Gradient-weighted Class Activate Mapping (Grad-CAM) [30] to extract attention maps and apply an ad-hoc threshold to generate bounding boxes from the attention maps.

Radiomic Features Extraction. The radiomic features are composed of the following categories:

- First-Order statistics features measure the distribution of voxel intensities within the bounding boxes. The features include energy (the measurement of the magnitude of voxel values), entropy (the measurement of uncertainty in the image values), and max/mean/median gray level intensity within the region of interest (ROI), etc.
- Shape-based features include features like Mesh Surface, Pixel Surface, Perimeter, and etc.
- Gray-level features include a gray-level features include a Gray Level Co-occurance Matrix (GLCM) features, a Gray Level Size Zone (GLSZM) features, a Gray Level Run Length Matrix (GLRLM) features, a Neighboring Gray Tone Difference Matrix (NGTDM) features, and a Gray Level Dependence Matrix (GLDM) features.

Given the original images and generated bounding boxes, we used the Pyradiomic tool to extract radiomic features [34].

3.3. Semi-Supervised Loss Function

Our framework is mixed with supervised classification and unsupervised contrastive learning. For the localization task, we use the knowledge-augmented contrastive loss for unsupervised contrastive learning. For the classification task, we could have used standard cross-entropy loss, but considering that the chest X-ray dataset is highly imbalanced, we instead find focal loss more helpful [25]. We briefly review the two loss functions below.

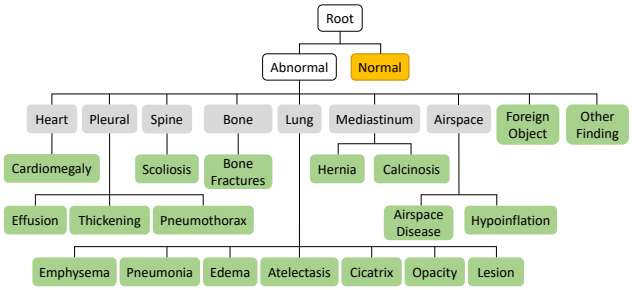


Figure 4. Disease hierarchy relationship predefined based on domain expertise, reprinted from [44].

Unsupervised Knowledge-Augmented Contrastive Loss. Our cross-modal contrastive loss function extends the normalized temperature-scaled cross-entropy loss (NT-Xent). We randomly sample a minibatch of N examples and define the contrastive prediction task on pairs of augmented examples derived from the minibatch. Let v_{bd} be the image in the minibatch with disease d and body part b, and $\mathrm{sim}(u, v)$ be the cosine similarity. The loss function $\ell_{v_{bd}}$ for a positive pair of example (v_{bd}, v'_{bd}) is defined as

$$\ell_{v_{bd}} = -\log \frac{\exp\left(\mathrm{sim}\left(\boldsymbol{z}_i(v_{bd}), \boldsymbol{z}_r(v'_{bd})\right)/\tau\right)}{\sum \mathbb{1}_{[k=b,l\neq d]} \exp\left(\mathrm{sim}\left(\boldsymbol{z}_i(v_{bd}), \boldsymbol{z}_i(v_{kd})\right)/\tau\right)}$$

where $\mathbb{1}_{[k=b,l\neq d]} \in \{0, 1\}$ is an indicator function evaluating to 1 iff $k = b$ and $l \neq d$. τ is the temperature parameter. The final unsupervised contrastive loss $\mathcal{L}_{cl}$ is computed across all disease-positive images in the minibatch.

Supervised Focal Loss. We feed the output of the image encoder f_i to a simple linear classifier. The supervised classification focal loss is defined as

$$\mathcal{L}_{fl} = \begin{cases} -\alpha\left(1-y'\right)^{\gamma}\log y', & y=1 \\ -(1-\alpha)y'^{\gamma}\log\left(1-y'\right), & y=0 \end{cases}$$

α allows us to give different importance to positive and negative examples. γ is used to distinguish easy and hard samples and force the model to learn more from difficult examples.

Eventually, we treat it as multi-task learning (one task is supervised disease classification and one is unsupervised contrastive learning) and the total loss is defined as

$$\mathcal{L} = \lambda \times \mathcal{L}_{cl} + (1-\lambda) \times \mathcal{L}_{fl}$$

4. Experiments

Dataset and Protocol Setting. We evaluated our framework using the NIH Chest X-ray dataset [35]. It contains 112,120 X-ray images collected from 30,805 patients. As other large chest X-ray datasets, this dataset is also extremely class imbalanced: the healthy cases (84,321 front-view images) are far more than cases with diseases (24,624

Method	Atelectasis	Cardiomegaly	Effusion	Infiltration	Mass	Nodule	Pneumonia	Pneumothorax	**Mean**
Wang et. al.[35]	0.72	0.81	0.78	0.61	0.71	0.67	0.63	0.81	0.718
Wang et. al.[36]	0.73	0.84	0.79	0.67	0.73	0.69	0.72	0.85	0.753
Yao et. al.[38]	0.77	0.90	0.86	0.70	0.79	0.72	0.71	0.84	0.786
Rajpurkar et. al.[28]	0.82	0.91	0.88	0.72	0.86	0.78	0.76	0.89	0.828
Kumar et. al.[18]	0.76	0.91	0.86	0.69	0.75	0.67	0.72	0.86	0.778
Liu et. al.[20]	0.79	0.87	0.88	0.69	0.81	0.73	0.75	0.89	0.801
Seyyed et. al.[31]	0.81	0.92	0.87	0.72	0.83	0.78	0.76	0.88	0.821
Our model	0.84	0.93	0.88	0.72	0.87	0.79	0.77	0.90	0.838

Table 1. Comparison with the baseline models for AUC of each class and average AUC. For each column, red values denote the best results.

front-view images), and different disease occurrence frequencies vary dramatically. The disease labels were extracted from radiology reports with a rule-based tool [26]. There are 9 classes, specifically one for "No findings" and 8 for diseases (Atelectasis, Cardiomegaly, Effusion, Infiltration, Mass, Nodule, Pneumonia, and Pneumothorax). The disease labels are expected to have above 90% accuracy. In addition, the dataset includes 984 bounding boxes for 8 types of chest diseases annotated for 880 images by radiologists. We separate the images with provided bounding boxes from the entire dataset. Hence, we have two sets of images called "annotated" (880 images) and "unannotated" (111,240 images).

In our experiment, we follow the same protocol of [35], to shuffle the unannotated dataset into three subsets: 70% for training, 10% for validation, and 20% for testing. For the annotated dataset, we randomly split the dataset into two subsets: 20% for training and 80% for testing. Note that there is no patient overlap between all the sets.

Evaluation Metrics. For the disease classification task, we use Area under the Receiver Operating Characteristic curve (AUC) to measure the performance of our model. For the disease localization task, we evaluate the detected regions against annotated ground truth bounding boxes, using intersection over union ratio (IoU). The localization results are only calculated on the test set of the annotated dataset. The localization is defined as correct only if IoU $>$ T(IoU), where T(*) is the threshold.

Implementation Details. We use the ResNet-18 model as the image encoder. We initialize the image encoder with the weights from the pre-trained ImageNet model except for the last fully-connected layer. We set the batch size as 64 and train the model for 30 epochs. We optimize the model by the Adam method and decay the learning rate by 0.1 from 0.001 every 5 epochs. Furthermore, we use linear warmup for the first 10 epochs only for the disease classification task, which helps the model converge faster to generate stable heatmaps. We train our model on AWS with one Nvidia Tesla V100 GPU. The model is implemented in PyTorch.

4.1. Disease Classification

Table 1 shows the AUC of each class and a mean AUC across the 8 chest diseases. Compared to a series of relevant baseline models, our proposed model achieves better AUC scores for the majority of diseases. The overall improvement in performance is remarkable when compared to other models except CheXNet [28]. One possible reason for our lack of improvement can be that [28]'s backbone is DenseNet-121, which is much deeper than the ResNet-18 in our model. It thus, able to capture much more discriminative features than our ResNet-18. Despite the fact, our model still achieves better or comparable results than CheXNet, which demonstrates that the cross-modal contrastive learning branch boosts the robustness of the image features without the need to increase the complexity of the backbone. Specifically, the performance of our model demonstrates significant improvements for disease abnormalities with larger associated regions on the image, such as "Ateclectasis", "Cardiomegaly", and "Pneumothorax". In addition, small objects features like "Mass" and "Nodule", are recognized as well as in CheXNet. In summary, these experimental results show the superiority of our proposed model over relevant other methodologies.

4.2. Disease Localization

We compare our disease localization accuracy to other state-of-the-art models under different IoU thresholds (Table 2). Since disease localization is not an easy task in chest X-ray images, we did not find as many other methods as for disease classification task. To our knowledge, we only have two baseline methods from [35] and [19]. From these comparisons, we find our model significantly outperforms baselines by an average of 2% over different IoU thresholds. Importantly, our model is able to perform well not only on the easier tasks, but also for more difficult ones like localizing "Mass" and "Nodule", where the disease localization is within a small area. When the IoU threshold is set to 0.1, our model outperforms others on all diseases except for "Cardiomegaly". As the IoU threshold increases, our framework is superior to other models in terms of better accuracy and maintains this superior performance. For

T(IoU)	Model	Atelectasis	Cardiomegaly	Effusion	Infiltration	Mass	Nodule	Pneumonia	Pneumothorax	**Mean**
0.1	*Wang et. al.*[35]	0.69	0.94	0.66	0.71	0.40	0.14	0.63	0.38	0.569
	Li et. al.[19]	0.71	0.98	0.87	0.92	0.71	0.40	0.60	0.63	0.728
	Our model	0.72	0.96	0.88	0.93	0.74	0.45	0.65	0.64	0.746
0.2	*Wang et. al.*[35]	0.47	0.68	0.45	0.48	0.26	0.05	0.35	0.23	0.371
	Li et. al.[19]	0.53	0.97	0.76	0.83	0.59	0.29	0.50	0.51	0.622
	Our model	0.55	0.89	0.78	0.85	0.62	0.31	0.52	0.54	0.633
0.3	*Wang et. al.*[35]	0.24	0.46	0.30	0.28	0.15	0.04	0.17	0.13	0.221
	Li et. al.[19]	0.36	0.94	0.56	0.66	0.45	0.17	0.39	0.44	0.496
	Our model	0.39	0.85	0.60	0.67	0.43	0.21	0.40	0.45	0.500
0.4	*Wang et. al.*[35]	0.09	0.28	0.20	0.12	0.07	0.01	0.08	0.07	0.115
	Li et. al.[19]	0.25	0.88	0.37	0.50	0.33	0.11	0.26	0.29	0.374
	Our model	0.24	0.81	0.42	0.54	0.34	0.13	0.28	0.32	0.385
0.5	*Wang et. al.*[35]	0.05	0.18	0.11	0.07	0.01	0.01	0.03	0.03	0.061
	Li et. al.[19]	0.14	0.84	0.22	0.30	0.22	0.07	0.17	0.19	0.269
	Our model	0.16	0.77	0.29	0.35	0.24	0.09	0.15	0.22	0.284
0.6	*Wang et. al.*[35]	0.02	0.08	0.05	0.02	0.00	0.01	0.02	0.03	0.029
	Li et. al.[19]	0.07	0.73	0.15	0.18	0.16	0.03	0.10	0.12	0.193
	Our model	0.09	0.74	0.19	0.16	0.18	0.04	0.11	0.14	0.206
0.7	*Wang et. al.*[35]	0.01	0.03	0.02	0.00	0.00	0.00	0.01	0.02	0.011
	Li et. al.[19]	0.04	0.52	0.07	0.09	0.11	0.01	0.05	0.05	0.118
	Our model	0.05	0.54	0.09	0.11	0.12	0.02	0.07	0.06	0.133

Table 2. Disease localization accuracy comparison under different IoU thresholds. Red numbers denote the best result for each column.

Method	Atelectasis	Cardiomegaly	Effusion	Infiltration	Mass	Nodule	Pneumonia	Pneumothorax	**Mean**
Base	0.75	0.85	0.83	0.67	0.69	0.64	0.70	0.79	0.740
w. FL	0.78	0.84	0.80	0.68	0.76	0.72	0.72	0.82	0.765
w. BYOP	0.82	0.90	0.85	0.71	0.82	0.75	0.74	0.86	0.806
Full model	0.84	0.93	0.88	0.72	0.87	0.79	0.77	0.90	0.838

Table 3. Ablation studies on focal loss and BYOP module for disease classification. Red numbers denote the best result for each column.

instance, when the threshold increases, the IoUs of "Cardiomegaly" decrease less than the baselines and even outperform the baselines when IoU threshold is above 0.5.

We prefer a higher IoU threshold, specifically, IoU = 0.7, for disease localization because we expect high-accuracy disease localization application is necessary for clinical applications. To this end, the method we propose is superior to the baseline by a slight margin.

It is also worth nothing that, for some diseases, such as Pneumonia and Infiltration, the localization of disease can appear in multiple places while only one bounding box is provided for each image. Hence, it is reasonable that our model does not align well with the ground truth when the threshold is as small as 0.1, especially for Pneumonia and Infiltration. Overall, our model outperforms the reference models for almost all IoU thresholds.

4.3. Ablation Discussion

In this section, we study the contribution of our BYOP module on both disease classification and localization tasks.

Disease Classification. For this task, note that the use of focal loss should also boost the model with the class-imbalanced chest X-ray dataset. Thus, we compare the performance of our base model with only focal loss (labeled "w. FL") or with only the BYOP module (labeled "w. BYOP"), respectively. As shown in Table 3, although both focal loss and BYOP improve the model performance, BYOP contributed more strongly. This stronger contribution is expected since BYOP tends to generate more robust radiomic features, which further reinforces the image encoder to focus on the image region that contains the targeted disease.

Disease Localization. Note that our base model is a ResNet-18 image encoder, which is not as powerful as CheXNet [28] with DenseNet-121. Thus we compare the performance of our model with CheXNet. As shown in Figure 5, our localization result is superior to the CheXNet. For the example of 'Atelectasis', 'Cardiomegaly', 'Effusion', 'Nodule', 'Pneumonia' and 'Pneumothorax', while the baseline model tends to focus on a large area of the image, our model precisely captures the correct disease location. For harder localization cases like 'Mass' and 'Nodule',

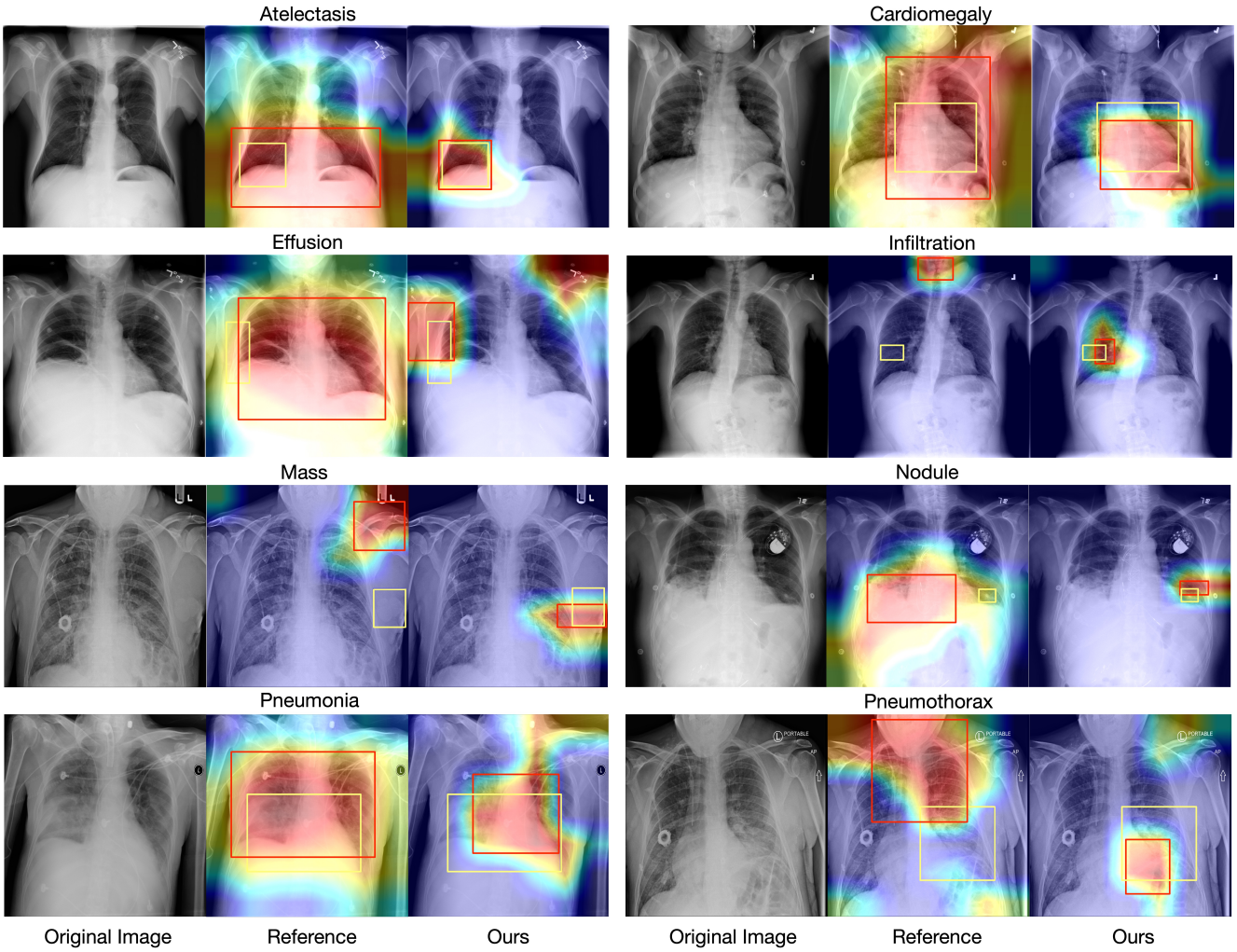


Figure 5. Examples of visualization of localization on the test images. We plot the results of diseases near thoracic. The attention maps are generated from the fourth layer of ResNet-18. The ground-truth bounding boxes and the predicted bounding boxes are shown in yellow and red, respectively. The left image in each pair is the original chest X-ray image, the middle one is the localization result of CheXNet [28] and the right one is our localization result. All examples are positive for corresponding disease labels. Best viewed in color.

the baseline model's focus is incorrect and does not have any overlap with the ground-truth areas while our model still predicts perfectly. The results demonstrate that the BYOP module significantly boosts the model performance.

5. Conclusion

In this work, we propose a semi-supervised, end-to-end knowledge-augmented contrastive learning model that can jointly model disease classification and localization with limited localization annotation data. Our approach differs from previous studies in the choice of data augmentation, the use of radiomic features as prior knowledge, and a feedback loop for image and radiomic features to mutually reinforce each other. Additionally, the project aims to address current gaps in radiology by making prior knowledge more accessible to image data analytic and diagnostic assisting tools, with the hope that this will increase the model's interpretability. Experimental results demonstrate that our method outperforms the state-of-the-art algorithms, especially for the disease localization task, where our method can generate more accurate bounding boxes. Importantly, we hope the method developed here is inspiring for the future research on incorporating different kinds of prior knowledge of medical images with contrastive learning.

Acknowledgement

This project is funded by Amazon Machine Learning Grant and NSF AI Center at UT Austin. It also was supported by the National Library of Medicine under Award No. 4R00LM013001.

References

[1] Wenjia Bai, Chen Chen, Giacomo Tarroni, Jinming Duan, Florian Guitton, Steffen E Petersen, Yike Guo, Paul M Matthews, and Daniel Rueckert. Self-supervised learning for cardiac mr image segmentation by anatomical position prediction. In *International Conference on Medical Image Computing and Computer-Assisted Intervention*, pages 541–549. Springer, 2019.

[2] David Bau, Bolei Zhou, Aditya Khosla, Aude Oliva, and Antonio Torralba. Network dissection: Quantifying interpretability of deep visual representations. In *Proceedings of the IEEE conference on computer vision and pattern recognition*, pages 6541–6549, 2017.

[3] Krishna Chaitanya, Ertunc Erdil, Neerav Karani, and Ender Konukoglu. Contrastive learning of global and local features for medical image segmentation with limited annotations. *arXiv preprint arXiv:2006.10511*, 2020.

[4] Ting Chen, Simon Kornblith, Mohammad Norouzi, and Geoffrey Hinton. A simple framework for contrastive learning of visual representations. In *International conference on machine learning*, pages 1597–1607. PMLR, 2020.

[5] Ting Chen, Simon Kornblith, Kevin Swersky, Mohammad Norouzi, and Geoffrey Hinton. Big self-supervised models are strong semi-supervised learners. *arXiv preprint arXiv:2006.10029*, 2020.

[6] Xinlei Chen, Haoqi Fan, Ross Girshick, and Kaiming He. Improved baselines with momentum contrastive learning. *arXiv preprint arXiv:2003.04297*, 2020.

[7] Xiaojian Chen, Kiyoko Oshima, Diane Schott, Hui Wu, William Hall, Yingqiu Song, Yalan Tao, Dingjie Li, Cheng Zheng, Paul Knechtges, et al. Assessment of treatment response during chemoradiation therapy for pancreatic cancer based on quantitative radiomic analysis of daily cts: An exploratory study. *PLoS One*, 12(6):e0178961, 2017.

[8] Carl Doersch, Abhinav Gupta, and Alexei A Efros. Unsupervised visual representation learning by context prediction. In *Proceedings of the IEEE international conference on computer vision*, pages 1422–1430, 2015.

[9] Armin Eilaghi, Sameer Baig, Yucheng Zhang, Junjie Zhang, Paul Karanicolas, Steven Gallinger, Farzad Khalvati, and Masoom A Haider. Ct texture features are associated with overall survival in pancreatic ductal adenocarcinoma–a quantitative analysis. *BMC medical imaging*, 17(1):1–7, 2017.

[10] Dumitru Erhan, Yoshua Bengio, Aaron Courville, and Pascal Vincent. Visualizing higher-layer features of a deep network. *University of Montreal*, 1341(3):1, 2009.

[11] Long Gao, Lei Zhang, Chang Liu, and Shandong Wu. Handling imbalanced medical image data: A deep-learning-based one-class classification approach. *Artificial Intelligence in Medicine*, 108:101935, 2020.

[12] Jean-Bastien Grill, Florian Strub, Florent Altché, Corentin Tallec, Pierre H Richemond, Elena Buchatskaya, Carl Doersch, Bernardo Avila Pires, Zhaohan Daniel Guo, Mohammad Gheshlaghi Azar, et al. Bootstrap your own latent: A new approach to self-supervised learning. *arXiv preprint arXiv:2006.07733*, 2020.

[13] Yan Han, Chongyan Chen, Ahmed H Tewfik, Ying Ding, and Yifan Peng. Pneumonia detection on chest x-ray using radiomic features and contrastive learning. *arXiv preprint arXiv:2101.04269*, 2021.

[14] Kaiming He, Haoqi Fan, Yuxin Wu, Saining Xie, and Ross Girshick. Momentum contrast for unsupervised visual representation learning. In *Proceedings of the IEEE/CVF Conference on Computer Vision and Pattern Recognition*, pages 9729–9738, 2020.

[15] Olle G Holmberg, Niklas D Köhler, Thiago Martins, Jakob Siedlecki, Tina Herold, Leonie Keidel, Ben Asani, Johannes Schiefelbein, Siegfried Priglinger, Karsten U Kortuem, et al. Self-supervised retinal thickness prediction enables deep learning from unlabelled data to boost classification of diabetic retinopathy. *Nature Machine Intelligence*, 2(11):719–726, 2020.

[16] Peng Huang, Seyoun Park, Rongkai Yan, Junghoon Lee, Linda C Chu, Cheng T Lin, Amira Hussien, Joshua Rathmell, Brett Thomas, Chen Chen, et al. Added value of computer-aided ct image features for early lung cancer diagnosis with small pulmonary nodules: a matched case-control study. *Radiology*, 286(1):286–295, 2018.

[17] Bingyi Kang, Yu Li, Zehuan Yuan, and Jiashi Feng. Exploring balanced feature spaces for rep-resentation learning.

[18] Pulkit Kumar, Monika Grewal, and Muktabh Mayank Srivastava. Boosted cascaded convnets for multilabel classification of thoracic diseases in chest radiographs. In *International Conference Image Analysis and Recognition*, pages 546–552. Springer, 2018.

[19] Zhe Li, Chong Wang, Mei Han, Yuan Xue, Wei Wei, Li-Jia Li, and Li Fei-Fei. Thoracic disease identification and localization with limited supervision. In *Proceedings of the IEEE Conference on Computer Vision and Pattern Recognition*, pages 8290–8299, 2018.

[20] Jingyu Liu, Gangming Zhao, Yu Fei, Ming Zhang, Yizhou Wang, and Yizhou Yu. Align, attend and locate: Chest x-ray diagnosis via contrast induced attention network with limited supervision. In *Proceedings of the IEEE/CVF International Conference on Computer Vision*, pages 10632–10641, 2019.

[21] Aravindh Mahendran and Andrea Vedaldi. Understanding deep image representations by inverting them. In *Proceedings of the IEEE conference on computer vision and pattern recognition*, pages 5188–5196, 2015.

[22] Ishan Misra and Laurens van der Maaten. Self-supervised learning of pretext-invariant representations. In *Proceedings of the IEEE/CVF Conference on Computer Vision and Pattern Recognition*, pages 6707–6717, 2020.

[23] Haidy Nasief, Cheng Zheng, Diane Schott, William Hall, Susan Tsai, Beth Erickson, and X Allen Li. A machine learning based delta-radiomics process for early prediction of treatment response of pancreatic cancer. *NPJ precision oncology*, 3(1):1–10, 2019.

[24] Mehdi Noroozi and Paolo Favaro. Unsupervised learning of visual representations by solving jigsaw puzzles. In *European conference on computer vision*, pages 69–84. Springer, 2016.

[25] Kitsuchart Pasupa, Supawit Vatathanavaro, and Suchat Tungjitnob. Convolutional neural networks based focal loss

for class imbalance problem: A case study of canine red blood cells morphology classification. *Journal of Ambient Intelligence and Humanized Computing*, pages 1–17, 2020.

[26] Yifan Peng, Xiaosong Wang, Le Lu, Mohammadhadi Bagheri, Ronald Summers, and Zhiyong Lu. NegBio: a high-performance tool for negation and uncertainty detection in radiology reports. In *AMIA Joint Summits on Translational Science proceedings. AMIA Joint Summits on Translational Science*, volume 2017, pages 188–196, 2018.

[27] Nicolas Pielawski, Elisabeth Wetzer, Johan Öfverstedt, Jiahao Lu, Carolina Wählby, Joakim Lindblad, and Nataša Sladoje. Comir: Contrastive multimodal image representation for registration. *arXiv preprint arXiv:2006.06325*, 2020.

[28] Pranav Rajpurkar, Jeremy Irvin, Kaylie Zhu, Brandon Yang, Hershel Mehta, Tony Duan, Daisy Ding, Aarti Bagul, Curtis Langlotz, Katie Shpanskaya, et al. Chexnet: Radiologist-level pneumonia detection on chest x-rays with deep learning. *arXiv preprint arXiv:1711.05225*, 2017.

[29] Joshua Robinson, Ching-Yao Chuang, Suvrit Sra, and Stefanie Jegelka. Contrastive learning with hard negative samples. *arXiv preprint arXiv:2010.04592*, 2020.

[30] Ramprasaath R Selvaraju, Abhishek Das, Ramakrishna Vedantam, Michael Cogswell, Devi Parikh, and Dhruv Batra. Grad-cam: Why did you say that? *arXiv preprint arXiv:1611.07450*, 2016.

[31] Laleh Seyyed-Kalantari, Guanxiong Liu, Matthew McDermott, and Marzyeh Ghassemi. Chexclusion: Fairness gaps in deep chest x-ray classifiers. *arXiv preprint arXiv:2003.00827*, 2020.

[32] Hannah Spitzer, Kai Kiwitz, Katrin Amunts, Stefan Harmeling, and Timo Dickscheid. Improving cytoarchitectonic segmentation of human brain areas with self-supervised siamese networks. In *International Conference on Medical Image Computing and Computer-Assisted Intervention*, pages 663–671. Springer, 2018.

[33] Yonglong Tian, Dilip Krishnan, and Phillip Isola. Contrastive representation distillation. In *International Conference on Learning Representations*, 2020.

[34] Joost JM Van Griethuysen, Andriy Fedorov, Chintan Parmar, Ahmed Hosny, Nicole Aucoin, Vivek Narayan, Regina GH Beets-Tan, Jean-Christophe Fillion-Robin, Steve Pieper, and Hugo JWL Aerts. Computational radiomics system to decode the radiographic phenotype. *Cancer research*, 77(21):e104–e107, 2017.

[35] Xiaosong Wang, Yifan Peng, Le Lu, Zhiyong Lu, Mohammadhadi Bagheri, and Ronald M Summers. Chestx-ray8: Hospital-scale chest x-ray database and benchmarks on weakly-supervised classification and localization of common thorax diseases. In *Proceedings of the IEEE conference on computer vision and pattern recognition*, pages 2097–2106, 2017.

[36] Xiaosong Wang, Yifan Peng, Le Lu, Zhiyong Lu, and Ronald M Summers. Tienet: Text-image embedding network for common thorax disease classification and reporting in chest x-rays. In *Proceedings of the IEEE conference on computer vision and pattern recognition*, pages 9049–9058, 2018.

[37] Yuzhe Yang and Zhi Xu. Rethinking the value of labels for improving class-imbalanced learning. *arXiv preprint arXiv:2006.07529*, 2020.

[38] Li Yao, Eric Poblenz, Dmitry Dagunts, Ben Covington, Devon Bernard, and Kevin Lyman. Learning to diagnose from scratch by exploiting dependencies among labels. *arXiv preprint arXiv:1710.10501*, 2017.

[39] Mang Ye, Xiangyuan Lan, Jiawei Li, and Pong Yuen. Hierarchical discriminative learning for visible thermal person re-identification. In *Proceedings of the AAAI Conference on Artificial Intelligence*, volume 32, 2018.

[40] Han Zhang, Jing Yu Koh, Jason Baldridge, Honglak Lee, and Yinfei Yang. Cross-modal contrastive learning for text-to-image generation. *arXiv preprint arXiv:2101.04702*, 2021.

[41] Richard Zhang, Phillip Isola, and Alexei A Efros. Colorful image colorization. In *European conference on computer vision*, pages 649–666. Springer, 2016.

[42] Yuhao Zhang, Daisy Yi Ding, Tianpei Qian, Christopher D Manning, and Curtis P Langlotz. Learning to summarize radiology findings. *arXiv preprint arXiv:1809.04698*, 2018.

[43] Yuhao Zhang, Hang Jiang, Yasuhide Miura, Christopher D Manning, and Curtis P Langlotz. Contrastive learning of medical visual representations from paired images and text. *arXiv preprint arXiv:2010.00747*, 2020.

[44] Yixiao Zhang, Xiaosong Wang, Ziyue Xu, Qihang Yu, Alan Yuille, and Daguang Xu. When radiology report generation meets knowledge graph. In *Proceedings of the AAAI Conference on Artificial Intelligence*, volume 34, pages 12910–12917, 2020.

[45] Zongwei Zhou, Vatsal Sodha, Md Mahfuzur Rahman Siddiquee, Ruibin Feng, Nima Tajbakhsh, Michael B Gotway, and Jianming Liang. Models genesis: Generic autodidactic models for 3d medical image analysis. In *International Conference on Medical Image Computing and Computer-Assisted Intervention*, pages 384–393. Springer, 2019.

[46] Jiuwen Zhu, Yuexiang Li, Yifan Hu, Kai Ma, S Kevin Zhou, and Yefeng Zheng. Rubik's cube+: A self-supervised feature learning framework for 3d medical image analysis. *Medical Image Analysis*, 64:101746, 2020.